

Refined modeling of superconducting double helical coils using finite element analyses

This article has been downloaded from IOPscience. Please scroll down to see the full text article.

2012 Supercond. Sci. Technol. 25 065006

(<http://iopscience.iop.org/0953-2048/25/6/065006>)

View [the table of contents for this issue](#), or go to the [journal homepage](#) for more

Download details:

IP Address: 130.251.168.1

The article was downloaded on 23/04/2012 at 15:49

Please note that [terms and conditions apply](#).

Refined modeling of superconducting double helical coils using finite element analyses

S Farinon and P Fabbriatore

INFN-Sezione di Genova, Via Dodecaneso, 33, 16146 Genova, Italy

E-mail: stefania.farinon@ge.infn.it

Received 24 January 2012, in final form 1 March 2012

Published 12 April 2012

Online at stacks.iop.org/SUST/25/065006

Abstract

Double helical coils are becoming more and more attractive for accelerator magnets and other applications. Conceptually, a sinusoidal modulation of the longitudinal position of the turns allows virtually any multipolar field to be produced and maximizes the effectiveness of the supplied ampere turns. Being intrinsically three-dimensional, the modeling of such structures is very complicated, and several approaches, with different degrees of complexity, can be used. In this paper we present various possibilities for solving the magnetostatic problem of a double helical coil, through both finite element analyses and direct integration of the Biot–Savart law, showing the limits and advantages of each solution and the corresponding information which can be derived.

(Some figures may appear in colour only in the online journal)

1. Introduction

In their many publications of the last decade [1–5], Meinke, Ball and Goodzeit demonstrated that the double helical coil (DHC) design is an interesting option to be considered for accelerator magnets. DHCs are basically composed of two concentric layers of solenoid coils with opposite currents and having helical turns modulated to produce the desired transverse field, the solenoid field being canceled. The main advantage of a DHC design is that the turn modulation can be arranged in such a way as to produce any superposition of field multipoles, providing a very powerful tool for designing combined function accelerator magnets. In particular the DHC layout can solve the difficult problem of how to arrange the focusing magnets very close each other in the interaction region of colliders. In this case it was demonstrated [6] that the turn path can be suitably modulated to cancel the strong cross-talk effects between the coils placed on the two beams.

Since the magnetic problem is basically 3D, the design of a DHC is not an easy task, especially if the coils are superconducting. In this case we not only need to precisely know the magnetic field generated in the bore, but also the peak field in the winding and the magnetic energy. The

main problem is strictly related to the layout of a DHC in which each turn has a complex geometry, requiring particular manufacturing methods. The most common technology involves the machining of cavities in a cylindrical shell. The cavities, hosting the superconducting wire, follow the path required by the field to be generated: elliptical for a dipole, sinusoidal modulated for multipoles. The geometrical field quality, a fundamental parameter for accelerator magnets, is determined by the precision of the machining. The drawback of this technical approach is that the overall current density is low, because a significant amount of winding space is in fact occupied by the cylinder itself, and consequently, in order to generate significant fields, the current density in the wire needs to be high. Briefly, the current density in the wire of a DHC is generally high not only because part of the current generates a self-canceling solenoid field, but also, and mainly, because the packing factor is limited by the need for a wire supporting structure, fundamental to the field quality.

An accurate magnetic computation of the peak field and the stored energy is extremely important for a superconducting coil. The peak field determines the margin of the magnet operation and needs to be precisely known. Two-dimensional approximations or computation with a

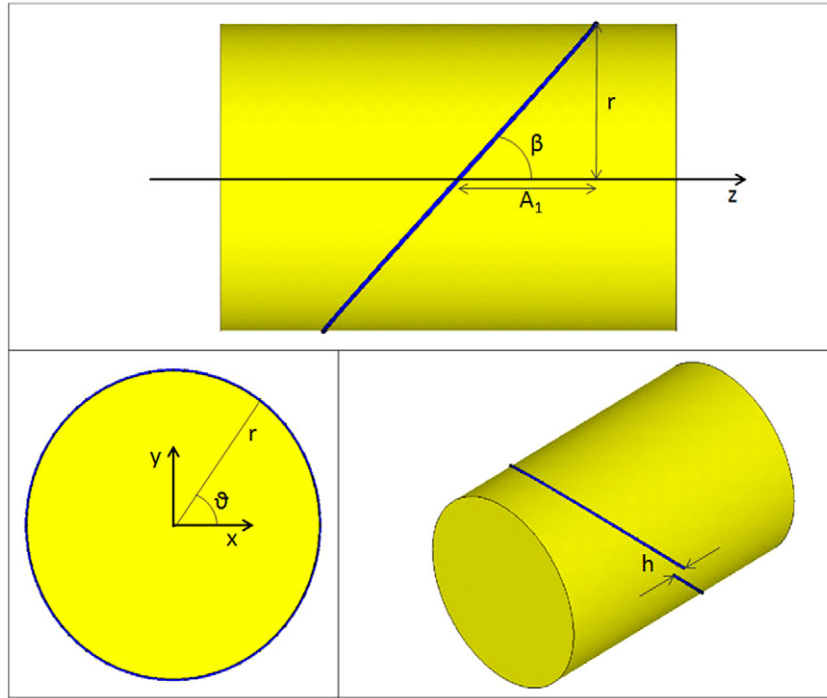


Figure 1. A single tilted elliptical turn wound onto a cylindrical mandrel, showing the definition of the helix parameters.

distributed current density may lead to under-evaluation of the peak field and the design of a magnet with a low margin; conversely the designers may be obliged to assume an unjustified reserve on the margin.

We have analyzed the problem through a comparative study of the different approaches to the magnetic field calculation of helical coils. Both 2D and 3D methods are studied, involving finite element (FE) analyses and numerical solutions based on Biot–Savart. We think that the result of this study will provide an effective tool to designers of superconducting double helical magnets.

2. General description of DHCs

2.1. Geometrical definition

The basic principle of a DHC is very simple. Let us consider, for instance, two solenoids obtained by winding tilted elliptical turns onto a cylindrical mandrel, with opposite tilt angles with respect to the central axis (see figures 1 and 2). If the current is flowing in opposite directions, we get a perfect transverse dipolar field, whilst the longitudinal components of the solenoid cancel each other out.

Following the formulation proposed by Meinke *et al* [3], the parametric equations of the two helices in Cartesian coordinates $\begin{matrix} x \\ y \\ z \end{matrix}$ can be written as:

$$\begin{cases} r \cos \vartheta \\ r \sin \vartheta \\ \frac{h\vartheta}{2\pi} + A_1 \sin \vartheta \end{cases} \quad \text{and}$$

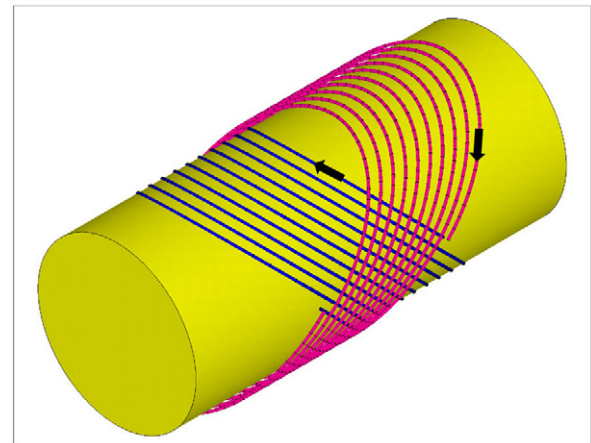


Figure 2. Two layers of tilted elliptical turns wound onto a cylindrical mandrel with opposite tilt angles with respect to the central axis, showing the current flow directions.

$$\begin{cases} r \cos \vartheta \\ r \sin \vartheta \\ \frac{h\vartheta}{2\pi} - A_1 \sin \vartheta, \end{cases} \quad -\pi N \leq \vartheta \leq \pi N \quad (1)$$

where h is the pitch of the helix, N is the number of turns of each layer and A_1 is connected to the tilt angle through:

$$\tan \beta = \frac{r}{\frac{h}{2\pi} + A_1}. \quad (2)$$

If $r \gg h$, which is nearly always true, $A_1 = r / \tan \beta$.

This principle can be easily extended to produce any multipolar field using the following equations for the two

helices:

$$\left\{ \begin{array}{l} r \cos \vartheta \\ r \sin \vartheta \\ \frac{h\vartheta}{2\pi} + A_n \sin n\vartheta \end{array} \right. \quad \text{and} \quad \left\{ \begin{array}{l} r \cos \vartheta \\ r \sin \vartheta \\ \frac{h\vartheta}{2\pi} - A_n \sin n\vartheta, \end{array} \right. \quad -\pi N \leq \vartheta \leq \pi N \quad (3)$$

where n is the order of the multipole. The resulting tilt angle is:

$$\tan \beta = \frac{r}{\frac{h}{2\pi} + nA_n}. \quad (4)$$

In real cases, the two helices represent concentric magnets, so that they cannot have the same radius. The correct mathematical treatment is then

$$\left\{ \begin{array}{l} r_1 \cos \vartheta \\ r_1 \sin \vartheta \\ \frac{h\vartheta}{2\pi} + A_{n1} \sin n\vartheta \end{array} \right. \quad \text{and} \quad \left\{ \begin{array}{l} r_2 \cos \vartheta \\ r_2 \sin \vartheta \\ \frac{h\vartheta}{2\pi} - A_{n2} \sin n\vartheta, \end{array} \right. \quad -\pi N \leq \vartheta \leq \pi N. \quad (5)$$

The two coefficients A_{n1} and A_{n2} can be determined, for example, by imposing the same inclination angle β to the two helices:

$$\tan \beta = \frac{r_1}{\frac{h}{2\pi} + nA_{n1}} = \frac{r_2}{\frac{h}{2\pi} + nA_{n2}}. \quad (6)$$

2.2. Magnetic field calculations using the Biot–Savart law

The magnetic field produced by the helices in (5) cannot be analytically determined. The problem can be approached through the Biot–Savart law, but a numerical integration has to be performed in order to get the results. In fact, the magnetic field generated by a current I flowing along a line ℓ can be determined using the Biot–Savart equation:

$$\vec{B} = \frac{\mu_0 I}{4\pi} \int_{\ell} \frac{d\vec{\ell} \times \vec{R}}{|R|^3} \quad (7)$$

where \vec{R} is the displacement vector from the line element to the point at which the field is being computed. In our case

$$d\vec{\ell}_1 = \left\{ \begin{array}{l} -r_1 \sin \vartheta \, d\vartheta \\ r_1 \cos \vartheta \, d\vartheta \\ \left(\frac{h}{2\pi} + nA_{n1} \cos n\vartheta \right) d\vartheta \end{array} \right. \quad \text{and} \quad d\vec{\ell}_2 = \left\{ \begin{array}{l} -r_2 \sin \vartheta \, d\vartheta \\ r_2 \cos \vartheta \, d\vartheta \\ \left(\frac{h}{2\pi} - nA_{n2} \cos n\vartheta \right) d\vartheta, \end{array} \right. \quad -\pi N \leq \vartheta \leq \pi N \quad (8)$$

$$\vec{R}_1 = \left\{ \begin{array}{l} x - r_1 \cos \vartheta \\ y - r_1 \sin \vartheta \\ z - \frac{h\vartheta}{2\pi} - A_{n1} \sin n\vartheta \end{array} \right. \quad \text{and} \quad \vec{R}_2 = \left\{ \begin{array}{l} x - r_2 \cos \vartheta \\ y - r_2 \sin \vartheta \\ z - \frac{h\vartheta}{2\pi} + A_{n2} \sin n\vartheta, \end{array} \right. \quad -\pi N \leq \vartheta \leq \pi N \quad (9)$$

$$\vec{B}(x, y, z) = \frac{\mu_0 I}{4\pi} \int_{-\pi N}^{\pi N} \left[\frac{d\vec{\ell}_1 \times \vec{R}_1}{|R_1|^3} - \frac{d\vec{\ell}_2 \times \vec{R}_2}{|R_2|^3} \right]. \quad (10)$$

Equation (10) can be numerically integrated to get the magnetic field produced by two concentric multipolar helical windings anywhere but along the helices themselves ($|R_1| = 0$ or $|R_2| = 0$), where equation (10) diverges. It is worth noting that equation (10) will be used to simulate the magnetic field produced by solid conductors, which are then represented through infinitely thin line currents lying on the conductor neutral axes: so we expect good accuracy in the magnetic field calculation far from the conductors themselves and a likely approximation by excess, due to the mentioned divergence, near the conductor surfaces, where the peak field is calculated.

2.3. Representations by FE modeling

Taking advantage of the flexibility of the FE code ANSYS [7], we can simulate a double helical magnet in several ways:

- a 2D analysis with the current density distributed following the desired multipole in the annulus representing the winding;
- a 3D analysis with the current density distributed following the desired multipole in the cylinder representing the winding;
- a 2D analysis representing the cross section of the real windings with a plane $z = \text{constant}$;
- a 3D magnetostatic scalar potential analysis with the real winding modeled through a primitive, consisting of predefined geometries, used to supply current source data to magnetic field problems and external to the FE mesh;
- a 3D magnetostatic vector potential analysis with the real winding modeled as an integral part of the FE mesh;
- a 3D analysis with the current distributed along the line representing the neutral axis of the conductor.

The magnetic field and the field harmonics computed through Biot–Savart integration can be considered as a reference for the FE analyses, whilst peak fields, inductance and stored energy calculations can only be used to make some comparisons and draw some conclusions.

3. Choice of a test case

In order to carry out and compare all the mentioned analyses, we need to identify a test case. We decided to concentrate on

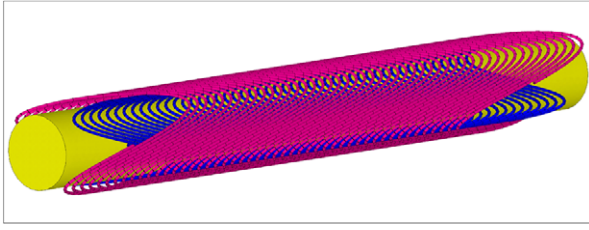


Figure 3. Sketch of the quadrupole which is being used as a test case for the FE analyses.

Table 1. Quadrupole characteristics.

Inner radius (r_1)	19.565 mm
Outer radius (r_2)	23.065 mm
Pitch (h)	6.4 mm
Number of turns (N)	48
Conductor dimensions	$1.53 \times 1.53 \text{ mm}^2$
Gradient	95.6 T m^{-1}
Current	2626 A
Tilt angle	14.1°
Magnetic length	0.3 m

one of the quadrupoles we are designing for the SuperB final doublet [6, 8, 9] whose characteristics are listed in table 1. It can be represented by the following equations:

$$\left\{ \begin{array}{l} r_1 \cos \vartheta \\ r_1 \sin \vartheta \\ \frac{h\vartheta}{2\pi} + \frac{r_1}{\tan \alpha} \sin 2\vartheta \end{array} \right. \quad \text{and} \quad \left\{ \begin{array}{l} r_2 \cos \vartheta \\ r_2 \sin \vartheta \\ \frac{h\vartheta}{2\pi} - \frac{r_2}{\tan \alpha} \sin 2\vartheta, \end{array} \right. \quad -\pi N \leq \vartheta \leq \pi N \quad (11)$$

where $\alpha = 27^\circ$ is around twice the tilt angle (see equation (6)). A sketch of the resulting quadrupole is shown in figure 3.

Combining equations (10) and (11), it is possible to derive analytically the resulting gradient far from the ends of the quadrupole. It is given by

$$G = \frac{\mu_0 I}{h \tan \alpha} \left(\frac{1}{r_1} + \frac{1}{r_2} \right) = 95.6 \text{ T m}^{-1}. \quad (12)$$

4. Biot–Savart numerical integration

The Biot–Savart integration has been performed numerically writing a specific code in Fortran, which simply performs the integrals in equation (10) through the trapezoidal rule with an integration step $\Delta\vartheta = 1^\circ$. Through this program it is possible to compute the three components of the magnetic field produced by the test quadrupole everywhere in the space but along the helices themselves, where, by definition, the magnetic field diverges. As an example, the black line in figure 4 represents the magnetic field along the 45° axis on

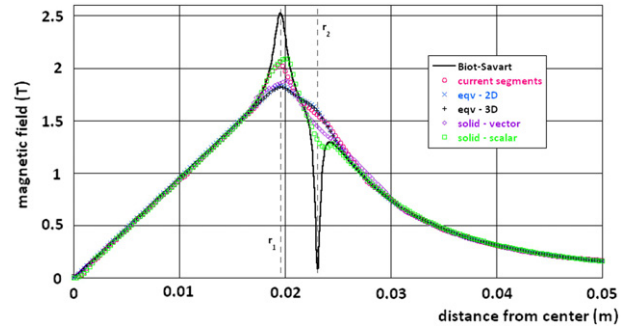


Figure 4. Magnetic field along the 45° axis on the $z = 0$ plane as a function of the distance from the origin of the axis calculated using the Biot–Savart integration and all the considered FE analyses.

the $z = 0$ plane as function of the distance from the origin of the axis. The divergence of the field around r_1 and r_2 , the radii of the helices, is clearly deducible. With a current of 2626 A, the gradient turns out to be 95.61 T m^{-1} , as designed.

In two dimensions, the field quality of a quadrupole magnet is usually expressed in terms of the skew (a_n) and normal (b_n) Fourier harmonic components, defined in units through the following relation [10]:

$$B_y + iB_x = 10^{-4} Gr_g \sum_{n=1}^{\infty} (b_n + ia_n) \left(\frac{x + iy}{r_g} \right)^{n-1} \quad (13)$$

where G is the nominal gradient and r_g is the radius of the good field region. The normal harmonic component in units turns out to be:

$$\begin{aligned} b_{n+1} &= \frac{10^4}{\pi Gr_g} \int_0^{2\pi} B_y(r_g, \vartheta) \cos(n\vartheta) d\vartheta \\ &= \frac{10^4}{\pi Gr_g} \int_0^{2\pi} B_x(r_g, \vartheta) \sin(n\vartheta) d\vartheta. \end{aligned} \quad (14)$$

This representation is only valid in the limit $B_z = 0$ (an infinitely long magnet) which is not generally true in three dimensions. Only particle tracking can answer for the global effect exerted by the generated magnetic fields on the accelerated beams. Nevertheless, if we suppose that the longitudinal components of the magnetic field are not sufficiently intense to move the beam out of the good field region, equation (14) still gives us useful information on the field quality in terms of well-known field harmonics. In figures 5 and 6 the normal field harmonics as a function of the longitudinal distance from the origin of the axis are shown, calculated using equation (14) and integrating, respectively, B_y and B_x . The good field region is supposed to be a disk, with a radius of 12 mm, lying on a plane at $z = \text{const}$. The normalization is $Gr_g = 95.6 \times 12 \times 10^{-3} = 1.1472 \text{ T}$, so that for a perfectly quadrupolar field we expect $b_2 = 10^4$ units. As foreseen, differences in harmonics higher than the quadrupole can be evidenced, due to the three-dimensionality of the problem. Nevertheless, it is important to notice that within our numerical precision we find

$$\int_{-\infty}^{\infty} b_n dz \leq 10^{-4} \text{ units m} \sim 0 \quad n > 2 \quad (15)$$

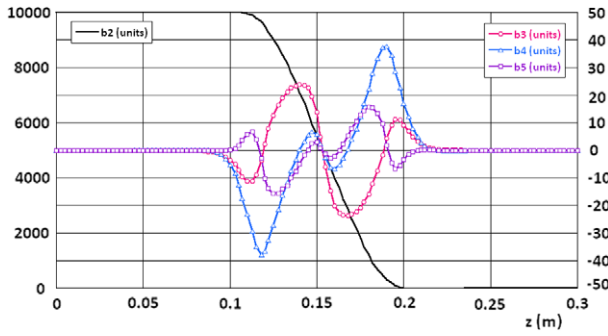


Figure 5. Field harmonics (units) from the Biot–Savart model as a function of the longitudinal distance from the axis origin, calculated integrating B_y in equation (13).

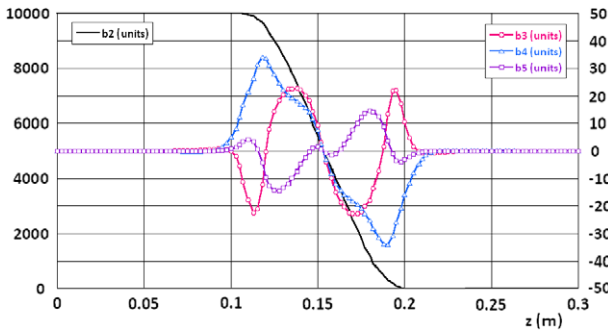


Figure 6. Field harmonics (units) from the Biot–Savart model as a function of the longitudinal distance from the axis origin, calculated integrating B_x in equation (13).

which implies that the overall effect of the higher harmonics is quite well compensated, if we consider a beam entering the quadrupole inside the good field region. From this point of view, the differences we find due to the computation procedure are not very important. However, in order to make meaningful comparisons with the next analyses, it is important to compare field harmonics calculated in the same way. For this reason, in the next paragraphs, when showing the field harmonics we refer to the integration in equation (14) solved through B_y .

The peak field is located along a line parallel to the axis of the magnet, at a radius r^* representing the external boundary of the winding of the inner layer and at 45° to the xy plane ($r^* = r_1 + r_0$, where $r_0 = 0.765$ mm is the radius of the conductor). The behavior of the magnetic field along this line is shown in figure 7. The peak is positioned near the first turn of the inner layer which is no longer covered by the outer layer and corresponds to 2.26 T. As anticipated in the previous paragraph, due to the divergence of the Biot–Savart integration around the neutral axis of the conductor, this value can only be interpreted as a superior limit for the peak field.

Inductance and then the stored magnetic energy can be calculated using

$$L = \frac{\sum_{i=1}^N \Phi_{B_i}}{I}, \quad E = \frac{1}{2} LI^2, \quad (16)$$

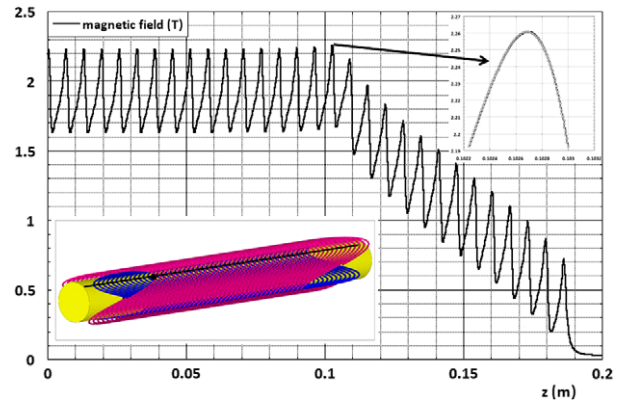


Figure 7. Magnetic field along a line parallel to the magnet axis, at a radius representing the external surface of the winding of the inner layer and at 45° to the xy plane, as shown in the picture.

that is via the determination of Φ_{B_i} , the magnetic flux through each single turn. Φ_{B_i} can be easily defined and calculated for a single planar turn, whilst additional effort is needed in our case, as the winding is a non-planar helix. To simplify the problem, first of all we need to transform the helical path in co-axial separated turns, so that Φ_{B_i} can be uniquely defined for each of them. The two helical layers can be then rewritten as

$$\left\{ \begin{array}{l} r_1 \cos \vartheta \\ r_1 \sin \vartheta \\ nh + \frac{r_1}{\tan \alpha} \sin 2\vartheta \end{array} \right. \quad \text{and} \quad \left\{ \begin{array}{l} r_2 \cos \vartheta \\ r_2 \sin \vartheta \\ nh - \frac{r_2}{\tan \alpha} \sin 2\vartheta, \end{array} \right. \quad -N \leq n \leq N-1, \quad 0 \leq \vartheta \leq 2\pi. \quad (17)$$

Since in our case $r_2 > r_1 \gg h$, we expect a negligible influence of this transformation on inductance and stored energy. With n ranging between $-N$ and $N-1$, equation (17) describes the $2N$ closed turns composing the double helical winding. To determine the magnetic flux intercepted by each of them, we can start from the consideration that the expression

$$\vec{S}_n(r, \vartheta) = \left\{ \begin{array}{l} r \cos \vartheta \\ r \sin \vartheta \\ nh + \frac{r}{\tan \alpha} \sin 2\vartheta, \end{array} \right. \quad -N \leq n \leq N-1 \quad (18)$$

represents $2N$ offset surfaces described through two parameters, r and ϑ . The flux Φ_B of the vector \vec{B} through a generic parameterized surface $\vec{S}(r, \vartheta)$ is a well-known quantity and can be expressed as

$$\Phi_B = \int_S \vec{B} \cdot (\vec{T}_r \cdot \vec{T}_\vartheta) dr d\vartheta \quad (19)$$

where $\vec{T}_r = \partial \vec{S} / \partial r$ and $\vec{T}_\vartheta = \partial \vec{S} / \partial \vartheta$.

Combining equations (18) and (19), the total magnetic flux Φ_B can be calculated as

$$\Phi_B = \sum_{n=-N}^{N-1} \int_0^r \int_0^{2\pi} \vec{B}_n(r, \vartheta, z_n) \cdot \left(-2r \frac{\sin^3 \vartheta}{\tan \alpha}; -2r \frac{\cos^3 \vartheta}{\tan \alpha}; r \right) dr d\vartheta \quad (20)$$

$$z_n = nh + \frac{r}{\tan \alpha} \sin 2\vartheta$$

where \vec{B}_n is the total magnetic field generated by the full set of turns in equation (17). Unfortunately, equation (20) cannot be applied in that form as there is no way, through this approach, to calculate exactly the field inside the conductors, especially at $r = r_1$ and r_2 where the Biot–Savart integral diverges. The simplest possibility to get an approximated solution is to linearly interpolate the magnetic field between the inner and outer boundary of the two layers:

$$\vec{B}_n^*(r, \vartheta, z_n) = \begin{cases} \vec{B}_n(r, \vartheta, z_n) & r < r_1 - r_0 \\ \vec{B}_n(r_1 - r_0, \vartheta, z_n) + \frac{\vec{B}_n(r_1 + r_0, \vartheta, z_n) - \vec{B}_n(r_1 - r_0, \vartheta, z_n)}{2r_0} (r - r_1 + r_0) & r_1 - r_0 < r < r_1 + r_0 \\ \vec{B}_n(r, \vartheta, z_n) & r_1 + r_0 < r < r_2 - r_0 \\ \vec{B}_n(r_2 - r_0, \vartheta, z_n) + \frac{\vec{B}_n(r_2 + r_0, \vartheta, z_n) - \vec{B}_n(r_2 - r_0, \vartheta, z_n)}{2r_0} (r - r_2 + r_0) & r_2 - r_0 < r < r_2 + r_0 \\ \vec{B}_n(r, \vartheta, z_n) & r > r_2 + r_0. \end{cases} \quad (21)$$

The two magnetic fluxes ‘seen’ by the two layers can then be calculated as

$$\Phi_{B1} = \sum_{n=-N}^{N-1} \int_0^{r_1} \int_0^{2\pi} \vec{B}_n^*(r, \vartheta, z_n) \cdot \left(2r \frac{\sin^3 \vartheta}{\tan \alpha}; 2r \frac{\cos^3 \vartheta}{\tan \alpha}; r \right) dr d\vartheta \quad (22)$$

$$\Phi_{B2} = \sum_{n=-N}^{N-1} \int_0^{r_2} \int_0^{2\pi} \vec{B}_n^*(r, \vartheta, z_n) \cdot \left(2r \frac{\sin^3 \vartheta}{\tan \alpha}; 2r \frac{\cos^3 \vartheta}{\tan \alpha}; r \right) dr d\vartheta. \quad (23)$$

The total flux $\Phi_B = \Phi_{B1} + \Phi_{B2}$ is 0.22 Wb, corresponding to an inductance of 0.17 mH and a stored energy of 0.58 kJ. For the same reasons as the peak field, we expect these values to be approximated by excess.

5. Finite element models

5.1. Equivalent FE 2D model with a $\cos 2\theta$ distribution of current density

An accurate 2D model of this kind of quadrupole is not possible, as there is not a repetitive cross section to be

reproduced with finite elements. A significant model is made by two concentric annuli, representing the volumes where the windings are deposited, in which a current density distributed as $J = J_0 \cos 2\vartheta$ flows, where ϑ is the polar angle on the xy plane. The resulting gradient can be obtained by integrating the gradient produced by an infinitely thin layer over r :

$$G = \int_{r_1-r_0}^{r_1+r_0} \frac{\mu_0 J_0}{2r^2} r dr + \int_{r_2-r_0}^{r_2+r_0} \frac{\mu_0 J_0}{2r^2} r dr = \frac{\mu_0 J_0}{2} \left[\ln \left(\frac{r_1 + r_0}{r_1 - r_0} \right) + \ln \left(\frac{r_2 + r_0}{r_2 - r_0} \right) \right]. \quad (24)$$

Given the desired quadrupole gradient of 95.6 T m⁻¹, equation (24) allows us to determine the required current density, which is $J_0 = 1.05 \times 10^9$ A m⁻². This model approximates the behavior of the test quadrupole far from the ends, around $z = 0$, so that all the harmonic components, except the quadrupole, are zero. The magnetic field along the 45° axis, shown in figure 4, is in good agreement with the Biot–Savart model in the central region and outside the magnet, whilst it is sensitively different within the windings, as in that region the magnetic field is highly affected by the type of model. The peak field is 1.83 T, less than the peak field coming from the Biot–Savart model, as expected. The calculated stored energy per unit length is 1.95 kJ m⁻¹, which, multiplied by the magnetic length, gives a total stored energy of $1.9486 \times 0.3 = 0.58$ kJ, corresponding to an inductance of 0.17 mH. Both stored energy and inductance are in agreement with those calculated using the Biot–Savart model.

5.2. Equivalent FE 3D model with a $\cos 2\theta$ distribution of current density

The previous 2D model can be easily extended to an equivalent 3D model by applying the same $\cos 2\vartheta$ distribution for the current density, uniformly in the longitudinal direction, to two concentric shells representing the volumes where the windings are deposited. The length of the shells can be set to the magnetic length of the quadrupole, 0.3 m. The results are very close being the same as those obtained through the 2D analysis: 1.83 T peak field, 0.57 kJ stored energy and 0.17 mH inductance. Figure 8 shows the behavior of b_2 and b_4 as function of the longitudinal distance from the origin of the axis as calculated with the Biot–Savart model and the 3D equivalent model. It is worth noting that all the odd harmonics of the equivalent model are zero because of the perfectly quadrupolar symmetry of the model itself. There is not a good agreement between the two results in figure 8, evidencing that the 3D equivalent model gives only a very coarse description of the test quadrupole, especially in the end zone. Therefore, the 3D equivalent model is quite useless, since the only valuable information can also be extracted from the 2D equivalent model.

5.3. A 2D analysis representing the cross section of the real windings with a plane $z = \text{constant}$

As mentioned above, the tilted helical windings do not have a repetitive cross section to be reproduced with FEs. However,

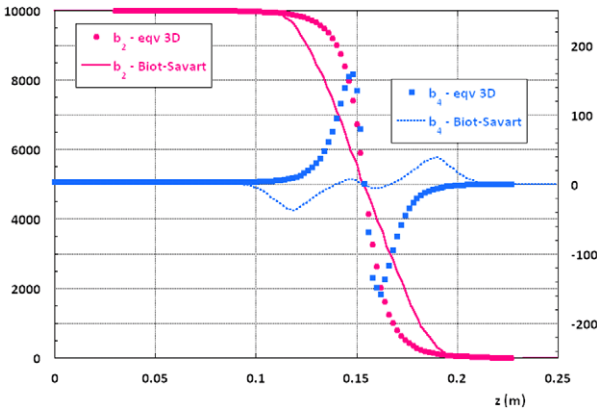


Figure 8. The first two even harmonics of the magnetic field (units) as calculated using the Biot–Savart model (plain and dotted lines) and the equivalent 3D model (full symbols).

another significant 2D model of these kinds of structures, although not truly representative, is given by the intersection of the windings with a plane at $z = \text{constant}$. Each surface resulting from that kind of intersection will have a current density given by the operating current divided by the area of the surface itself. Clearly, this approach will not satisfactorily describe the field quality, as each single section will not produce a fully quadrupolar field. Nevertheless, it can give a better description of the peak field with respect to the previous 2D analysis, without the need for an *ad hoc* current density. With a current of 2626 A the resulting gradient is nearly the designed value, 95.6 T m^{-1} . The peak field is found to be in the range 2.1–2.4 T, which is slightly more than that calculated through the Biot–Savart integration: the peak field is enhanced by the fact that each 2D analysis is representative of a 3D model whose geometry has no longitudinal variation. In all the considered sections, the total stored energy is 0.58 kJ, corresponding to an inductance of 0.17 mH.

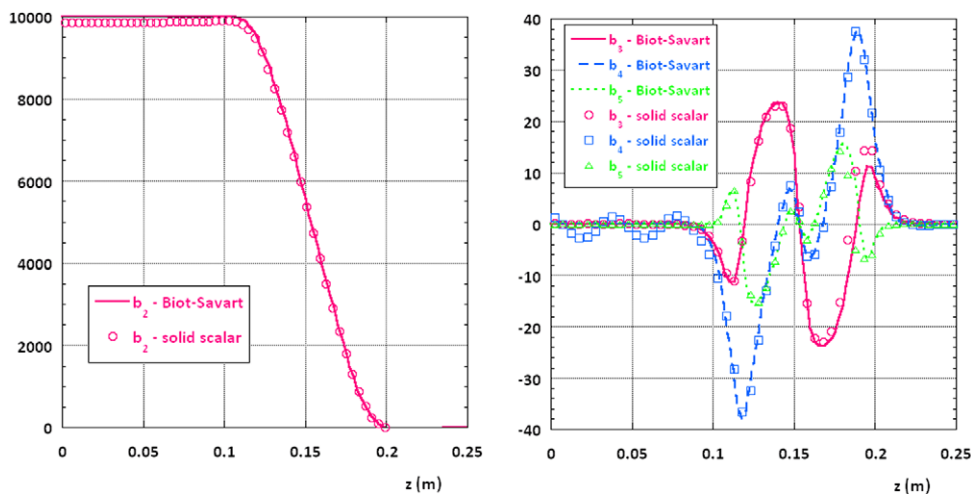


Figure 9. Quadrupole (left) and first three higher harmonics (right) of the magnetic field (units) as calculated using the Biot–Savart model (plain and dotted lines) and the magnetic scalar potential model (empty symbols).

5.4. Solid FE 3D model solved through scalar potential

The 3D magnetostatic analyses solved through scalar potential equations present a remarkable advantage: current sources do not have to be an integral part of the FE mesh, i.e. the scalar approach allows modeling of current sources as primitives (coils, bars and arcs) rather than FEs. These primitives, modeled through a special element, are used to represent the shape and location of current sources. The currents are then used to calculate the magnetic field intensity using a numerical integration technique involving the Biot–Savart law. For this reason, this formulation presents an analogous problem of accuracy to the direct integration of the Biot–Savart law in the determination of the magnetic field on conductors. In confirmation, figure 4 shows that the magnetic field along the 45° axis on the $z = 0$ plane calculated using the magnetic scalar potential formulation best agrees with the Biot–Savart integration with respect to the other considered formulations. Also, the harmonic components of the magnetic field, shown in figure 9, despite a small oscillation of the octupole, are in quite good agreement with the Biot–Savart integration. The peak field is 2.23 T, to be compared with the 2.26 T calculated through the direct integration. Finally, stored energy and inductance are respectively 0.55 kJ and 0.16 H.

5.5. Solid FE 3D model solved through a vector potential

The 3D vector potential approach is the most time consuming. Indeed, it requires that the conductors be an integral part of the meshed volumes, which is quite difficult when dealing with very complicated structures. This formulation presents another additional difficulty. In order to carry out a correct electromagnetic analysis, the continuity equation must be satisfied and the current density must be solenoidal (i.e. $\nabla \cdot \vec{J} = 0$). This means that the current density must satisfy the continuity law, or, in other words, the current density cannot have sources or sinks. Two-dimensional planar

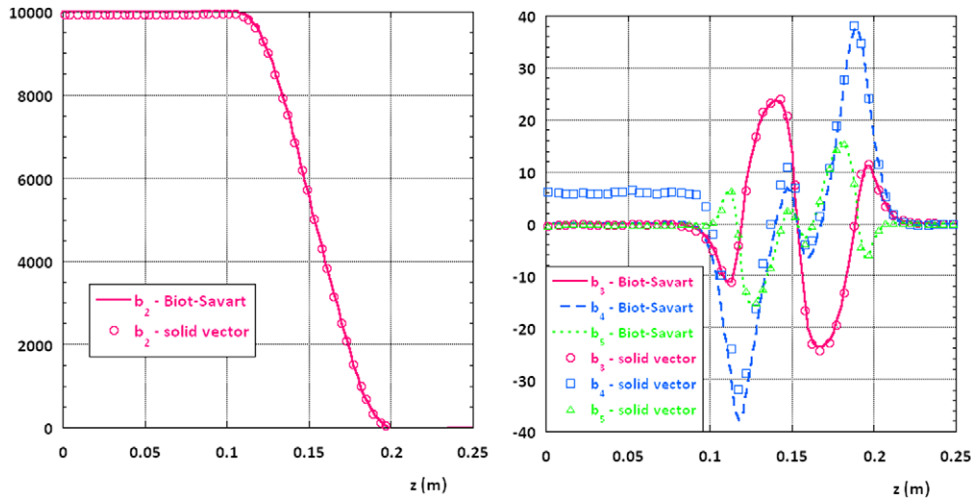


Figure 10. Quadrupole (left) and first three higher harmonics (right) of the magnetic field (units) as calculated using the Biot–Savart model (plain and dotted lines) and the magnetic vector potential model (empty symbols).

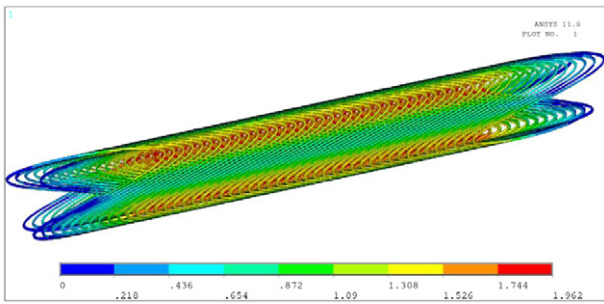


Figure 11. Magnetic field on conductors as calculated through the vector potential magnetostatic analysis.

and axisymmetric problems and 3D problems involving closed circuits automatically satisfy this solenoidal condition. However, general 3D problems do not automatically satisfy this condition and we need to verify that the solenoidal condition is satisfied when prescribing the source current density. To make sure that the applied current density is solenoidal, the procedure is to first perform a preliminary static electric current conduction analysis to obtain the current densities and then bring them into the magnetic analysis directly, applying the calculated current density loads. The resulting harmonic components of the magnetic field, compared with the Biot–Savart integration, are shown in figure 10. The only significant difference is the offset in the octupole component: this shift is strongly connected to the mesh size inside the quadrupole and could then be related to the accuracy of fulfilment of the solenoidal condition. The peak field, gathered from the magnetic field map shown in figure 11, is 1.96 T, which, as expected, is less than the value obtained through direct integration and is probably a better approximation of the real value. Stored energy and inductance are respectively 0.56 kJ and 0.16 H.

Finally, this approach, the most complicated one from the point of view of the modeling, has a great advantage: the same FE model, changing the element type and excluding meshed

air, can be used for mechanical analysis, directly applying Lorentz forces coming from the electromagnetic analysis, and also for stability and quench analyses. None of the previously described modeling techniques can be adapted in the same straightforward way.

5.6. Finite element 3D model with helical current segments

This infrequently used and undocumented load type applies current loads directly to meshed nodes, without the need for mesh specific volumes of conductors. The advantage is that the FE model is very simple: we only need to create a generic air volume, mesh it with a mesh size able to account for the pitch of the helix, and finally slightly move a predefined number of nodes in positions lying on the helix itself. Those nodes will directly carry the current loads. Unfortunately, the usefulness of this model is very limited. Actually, except for the quadrupole gradient, all the other parameters we are comparing can hardly be extracted. First of all, the peak field cannot even be estimated: the magnetic field on the nodes carrying the current being theoretically infinite, the calculated maximum fields depend on the dimension of the elements surrounding those nodes, where the nodal fields are averaged. This implies that the finer the mesh the higher the peak field. For the same reasons, the calculated stored energy and inductance are much higher than the correct values, 0.69 kJ and 0.20 mH, respectively. Since the stored energy is calculated by integrating the square of the magnetic field over all the modeled volumes, an approximated value can be obtained removing all the elements containing current nodes from the integration. In this way we find a stored energy of 0.54 kJ and a corresponding inductance of 0.16 mH, values closer to the other models.

Finally, the harmonics, shown in figure 12, are very noisy and suffer from the same kind of problem as the vector potential formulation: here the continuity equation is not even checked, so that a significant offset of the even harmonics in the central part of the magnet is found.

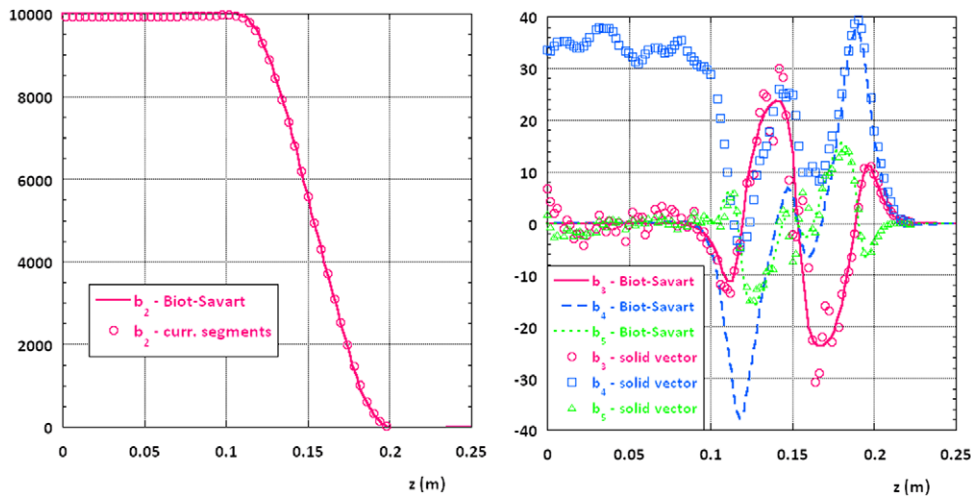


Figure 12. Quadrupole (left) and first three higher harmonics (right) as calculated through the Biot–Savart model and the 3D FE analysis using current segments.

Table 2. Comparison of the models.

Model	Gradient ($T\ m^{-1}$)	Peak field (T)	Stored energy (kJ)	Inductance (mH)	Number of nodes (millions)	CPU time- solution only (h)
Biot–Savart	95.61	2.26	0.58	0.17	—	~1
Equivalent 2D	95.60	1.83	0.58	0.17	0.2	≪1
Equivalent 3D	95.67	1.83	0.57	0.17	0.3	2
$z = \text{const.}$ cross sections	~95.6	2.34	0.57–0.58	0.17	0.2	≪1
3D vector potential	94.86	1.96	0.55	0.16	1.6	20
3D scalar potential	94.28	2.23	0.56	0.16	1.6	19
Current segments	94.89	—	0.69/0.54	0.20/0.16	0.3	2

6. Comparison of the models

The main results of all the models considered are summarized in table 2. This allows us to making a sort of cross-check among them: in fact, whilst the Biot–Savart integration can be considered as a reference for the determination of the harmonic content of the magnetic field, the FE analyses are in general more reliable for determining stored energy, inductance and peak field.

The first remark is that the equivalent models, both 2D and 3D, are quite easy and quick to perform, but not very useful: current density is calculated to match the quadrupole, peak field is under-estimated, stored energy and inductance are slightly over-estimated and finally harmonics are not in good agreement with direct integration. Also, the other 2D model, obtained by intersecting the quadrupole with $z = \text{const}$ planes, has the advantage that the required input data are the real currents circulating in the magnet, but all the other parameters are not very well matched.

Among the other 3D models, the current segments method is the fastest but gives quite uncertain results, so it is not advisable to use it in preference to any other approach.

A serious comparison can only be made between the Biot–Savart integration and the 3D FE model solved through either the scalar potential or the vector potential approach. Obviously, the direct integration has the advantage of being largely the fastest: our opinion is that it is an indispensable

approach, especially as it supplies a versatile tool to adjust the main parameters of the design. Once the main parameters have been fixed, it could be helpful to run a 3D FE model, as it allows confirmation of the direct integration results and their display in a more immediately readable way, through colored maps. If further analyses are not foreseen, the scalar potential is the best choice, as the FE model can be built quite easily. The vector potential method is the more logical approach only if a thermal or a mechanical analysis needs to be tackled afterwards: a FE model is much more difficult but it will be ‘recycled’ in the next analyses.

7. Conclusions

Exploiting the flexibility of the FE code ANSYS, we compared six different FE models with the direct Biot–Savart integration in terms of the main quantities which can be obtained from a static electromagnetic analysis of a particular double helical quadrupole chosen as a test case. The main conclusion is that direct Biot–Savart integration is the best choice for gathering all the information in the shortest time: the harmonic content of the magnetic field, peak field, stored energy and inductance. In cases where further analyses are needed, like structural or quench analyses, the 3D vector potential approach is advisable, as the same FE model of the electromagnetic analysis can be adapted to solve the other types of problems.

References

- [1] Meinke R B, Ball M J and Goodzeit C L 2003 Superconducting double-helix accelerator magnets *Proc. 2003 Particle Accelerator Conf. (Portland, OR, May 2003)* pp 1996–8 <http://accelconf.web.cern.ch/AccelConf/p03/PAPERS/WPAE025.PDF>
- [2] Goodzeit C L, Ball M J and Meinke R B 2003 The double-helix dipole—a novel approach to accelerator magnet design *IEEE Trans. Appl. Supercond.* **13** 1365–8
- [3] Meinke R B, Goodzeit C L and Ball M J 2003 Modulated double-helix quadrupole magnets *IEEE Trans. Appl. Supercond.* **13** 1369–72
- [4] Goodzeit C, Meinke R and Ball M 2007 Combined function magnets using double-helix coils *Proc. 2007 Particle Accelerator Conf. (Albuquerque, NM, June 2007)* pp 560–2 <http://accelconf.web.cern.ch/AccelConf/p07/PAPERS/MOPAS055.PDF>
- [5] Meinke R B, Lammers J, Masson P J and Stelzer G 2009 Direct double-helix magnet technology *Proc. 2009 Particle Accelerator Conf. (Vancouver, May 2009)* pp 229–31
- [6] Paoloni E, Bettoni S, Biagini M E and Raimondi P 2009 Magnetic design studies for the final focus quadrupoles of the super B large crossing angle collision scheme *Proc. 2008 Particle Accelerator Conf. (Genoa, June 2008)* pp 2401–3 <http://accelconf.web.cern.ch/AccelConf/e08/papers/wepd002.pdf>
- [7] ANSYS Multiphysics Release 11, ANSYS Inc.
- [8] Paoloni E, Bettoni S, Biagini M E, Raimondi P and Sullivan M 2009 Advances in the studies of the magnetic design for the final focus quadrupoles of the superB *Proc. 2009 Particle Accelerator Conf. (Vancouver, May 2009)* pp 238–40 <http://accelconf.web.cern.ch/AccelConf/PAC2009/papers/mo6pfp045.pdf>
- [9] Paoloni E *et al* 2011 Advances in the design of the superB final doublet *Proc. 2011 Int. Particle Accelerator Conf. (New York, Mar.–Apr. 2011)* pp 2454–6 <http://accelconf.web.cern.ch/AccelConf/IPAC2011/papers/wepo026.pdf>
- [10] Jain A K 1998 Basic theory of magnets *CERN Yellow Report 98–05* <http://cdsweb.cern.ch/record/1246515/files/p1.pdf>